

High-Reynolds-number wall-modelled large eddy simulations of turbulent pipe flows using explicit and implicit subgrid stress treatments within a spectral element solver

E. Ferrer^{a,*}, N. Saito^b, H.M. Blackburn^c, D.I. Pullin^b

^a ETSIAE-UPM - School of Aeronautics, Universidad Politécnica de Madrid, Plaza Cardenal Cisneros 3, Madrid E-28040 Spain

^b Graduate Aerospace Laboratories, California Institute of Technology, CA 91125 USA

^c Department of Mechanical and Aerospace Engineering, Monash University, Vic 3800, Australia

ARTICLE INFO

Article history:

Received 3 September 2018

Revised 23 June 2019

Accepted 15 July 2019

Available online 31 July 2019

Keywords:

Turbulent pipe flow

Large eddy simulation

Stretched-vortex model

Chung & Pullin model

Spectral vanishing viscosity (SVV)

Wall model

Virtual-wall model

ABSTRACT

We present explicit and implicit large eddy simulations for fully developed turbulent pipe flows using a continuous-Galerkin spectral element solver. On the one hand, the explicit stretched-vortex model (by Misra and Pullin [45] and Chung and Pullin [14]), accounts for an explicit treatment of unresolved stresses and is adapted to the high-order solver. On the other hand, an implicit approach based on a spectral vanishing viscosity technique is implemented. The latter implicit technique is modified to incorporate Chung & Pullin virtual-wall model instead of relying on implicit dissipative mechanisms near walls. This near-wall model is derived by averaging in the wall-normal direction and relying in local inner scaling to treat the time-dependence of the filtered wall-parallel velocity. The model requires space-time varying Dirichlet and Neumann boundary conditions for velocity and pressure respectively. We provide results and comparisons for the explicit and implicit subgrid treatments and show that both provide favourable results for pipe flows at $Re_\tau = 2 \times 10^3$ and $Re_\tau = 1.8 \times 10^5$ in terms of turbulence statistics. Additionally, we conclude that implicit simulations are enhanced when including the wall model and provide the correct statistics near walls.

© 2019 Elsevier Ltd. All rights reserved.

1. Introduction

Wall bounded flows and particularly pipe flows under fully developed turbulent conditions have attracted the interest of the scientific community for decades. Since the pioneering work of Reynolds [53], it was understood that the flow in pipes undergoes transition to turbulence at Reynolds numbers that are commonly found in engineering applications such as oil or water pipelines. The main characteristics of pipe flows have been compiled in by Smits et al. [59].

The accurate prediction of turbulence and associated statistic in pipes has fascinated scientists that study flow structures or design turbulence models, but also attracted the interest of engineers that need to account for energy losses and seek drag reduction techniques in long pipelines. To compute pipe flows and understand its physics, scientists have used direct numerical simulations (DNS) for low Reynolds numbers and large eddy simulations (LES) for large Reynolds numbers, which would otherwise require an extremely

fine mesh. The LES approach considers spatial filtering where the large structures are resolved, reducing modeling to the small turbulent structures (i.e. small eddies), which are considered to behave in an isotropic fashion (see the monograph by Sagaut [54]). Filtering enables scale separation: large scales (i.e. large eddies) to be resolved and small scales (i.e. subgrid-scale or SGS) to be modelled. While DNS methods enable accurate computations of all dynamically relevant scales present in the flow with a significant computational cost, LES allows affordable computations while providing accurate computation of scales of engineering relevance (i.e. large scales). See [16,54] for a summary of techniques to compute turbulent flows.

The constant increase in computational power has enabled simulations of DNS and LES for pipe flows for increasing Reynolds numbers. Various DNS at moderate Reynolds numbers ($Re_\tau = 500$ to 3000) have been reported [1,11–13,36,39,63] but are low compared to pipe flow experiments and pipe flows of engineering relevance [21,46,48,65], (e.g. $Re_\tau = 10^3$ to 10^5). At the time of writing, the highest Reynolds number LES of turbulent pipe flows is $Re_\tau = 2200$, described by Berrouk et al. [4]. LES for lower Reynolds numbers have been proposed in [8,15,23,22].

* Corresponding author.

E-mail address: esteban.ferrer@upm.es (E. Ferrer).

Explicit LES techniques derive subgrid models by introducing filtering into the Navier–Stokes (NS) equations to then model unresolved terms. Multiple filters and subgrid models have been proposed [54]. In this work, we select the “stretched-vortex model” (SVM) approach, which has been proposed by Misra and Pullin [45] and Chung and Pullin [14], henceforth referred to as SVM. This model, which will be detailed later, models the unresolved subgrid vorticity, in each cell, as a superposition of stretched vortices, each unidirectional and of “cylindrical” type. Extensions of the model to account for complex physics may be found in [56,57] for smooth and rough-wall channel flows, in [26,27] for turbulent boundary-layer flows, in [28] for attached-flow under adverse pressure gradients or more recently in [9,10] for detached flows.

Alternatively, implicit LES [6,20] use the numerical dissipation inherited from the numerical scheme (e.g. from upwinding the non-linear terms or finite element stabilization terms) to account for subgrid effects and hence do not require an explicit modelling of the unresolved terms. Implicit methods have seen an increased popularity when combined with high-order numerical techniques, e.g. [3,17], which show dissipation and dispersion errors that are confined to high wave number ranges hence limiting the numerically added dissipation to only weakly-resolved regions [2,19,24,42,47,58]. Among the existing implicit techniques, the spectral vanishing viscosity (SVV) method (e.g. see [30,34,37]) introduces an additional dissipative term (only to the highest wavenumbers) that enhances stability, vanishes in the laminar limit and provides spectrally accurate solutions (i.e. maintains exponential convergence in high order methods).

Explicit and implicit LES techniques may not provide the correct behaviour near the wall. One possibility is to increase the mesh resolution near the wall such that DNS solutions are obtained near walls. This approach has been reported by Chin et al. [12] for pipe flow but the authors only achieved a reduction of $\mathcal{O}(10)$ with respect to fully resolved DNS for $Re_\tau = 1000$. A different approach considers wall functions to relax the mesh constraint near walls. As explained by Piomelli and Balaras [51] and Piomelli [50], there is a huge potential when using wall models in LES since the number of required grid points, to fully resolve the inner layer, scales with streamwise-distance (z) based Reynolds number Re_z as $Re_z^{2.4}$. Wall modelling is therefore a practical necessity to apply LES to high Reynolds number flows to obtain a weak dependence on Re_z . Both explicit and implicit LES techniques proposed in this work include wall models. See [7,38,51,60] for reviews of wall models in LES.

This work is composed of three contributions. First, we adapt the stretched-vortex model SVM to a high-order continuous-Galerkin solver to compute pipe flows. Second, we extend the idea of distinguishing between near-wall and far-wall regions to implicit LES methods. We use a high-order SVV technique to compute the far region, while the near wall is modelled using SVM’s wall model: the virtual-wall model (VWM). To the authors’ knowledge, the combination of SVV and wall modelling has not been attempted before. Third, we compute turbulent pipe flow using both methods and compare the results for $Re_\tau = 2 \times 10^3$ and 1.8×10^5 to experimental data. Two main findings are detailed. First, the SVM is capable of predicting the turbulence statistics accurately even at high Reynolds numbers and second, the SVV method (no wall modelling) provides accurate enough statistics but is over-dissipative if compared to the proposed SVV method with wall-models.

The rest of the paper is organized as follows. First, we introduce the numerical methodology with emphasis on the SVM adapted to the high-order h/p solver, the SVV technique and the near wall treatment. Second, we compare results for explicit and implicit methods to experimental data. We finalize the paper with conclusions.

2. Methodologies

We start by summarising the h/p high-order technique and then incorporate the stretched-vortex model. We additionally provide details on the SVV technique and the virtual-wall model).

2.1. High order h/p spectral method using Semtex

Both explicit and implicit LES techniques described herein have been implemented in the framework provided by the parallel Galerkin spectral element–Fourier code Semtex [5]. We summarise here the main characteristics to then detail the required modifications to compute LES flows. The incompressible NS equations can be written as:

$$\frac{\partial \mathbf{u}}{\partial t} + \mathbf{N}(\mathbf{u}) = -\nabla p + \nu \nabla^2 \mathbf{u} + \mathbf{f}, \quad \nabla \cdot \mathbf{u} = 0, \quad (2.1)$$

where $\mathbf{u} = (u, v, w)^T$ represents the flow velocity vector, p is the ratio of pressure to fluid density, ν is the kinematic viscosity and \mathbf{f} an arbitrary body force. Eq. (2.1) introduces a general description for the non-linear terms $\mathbf{N}(\mathbf{u})$. The baseline “standard” Semtex formulation (without turbulence model) uses the skew-symmetric formulation:

$$\mathbf{N}(\mathbf{u}) = 1/2((\mathbf{u} \cdot \nabla) \mathbf{u} + \nabla \cdot (\mathbf{u} \otimes \mathbf{u})). \quad (2.2)$$

This form is preferred for its stability properties, in that it minimises aliasing errors as shown by Zang [62]. Additionally, Zang proposed an alternative skew-symmetric form, which is less expensive and is obtained when combining the convective form: $(\mathbf{u} \cdot \nabla) \mathbf{u}$, and divergence form: $\nabla \cdot (\mathbf{u} \otimes \mathbf{u})$, on alternate time steps, such that after two time steps, the skew-symmetric formulation, Eq. (2.2), is recovered. We favour the alternative form since it provides stable turbulent solutions at a reduced cost.

Eq. (2.1) is integrated in time using a stiffly-stable scheme with coefficients γ_0 , α_n and β_n , where the non-linear terms are treated explicitly while pressure and viscous terms are treated implicitly

$$\frac{\gamma_0 \mathbf{u}^{n+1} - \sum_{q=0}^{J-1} \alpha_q \mathbf{u}^{n-q}}{\Delta t} + \sum_{q=0}^{J-1} \beta_q [\mathbf{N}(\mathbf{u}^{n-q}) + \mathbf{f}^{n-q}] = -\nabla p^{n+1} + \nu \nabla^2 \mathbf{u}^{n+1}. \quad (2.3)$$

The resulting equation is separated using an intermediate variable $\hat{\mathbf{u}}$ into four steps: an explicit non-linear advection, an implicit pressure solve (Poisson equation) and an implicit velocity correction (Helmholtz equation), resulting in the scheme

$$\frac{\gamma_0 \hat{\mathbf{u}} - \sum_{q=0}^{J-1} \alpha_q \mathbf{u}^{n-q}}{\Delta t} = -\sum_{q=0}^{J-1} \beta_q [\mathbf{N}(\mathbf{u}^{n-q}) + \mathbf{f}^{n-q}], \quad (2.4)$$

$$-\nabla^2 p^{n+1} = -\frac{\gamma_0}{\Delta t} \nabla \cdot \hat{\mathbf{u}}, \quad (2.5)$$

$$\left(-\nabla^2 + \frac{\gamma_0}{\nu \Delta t}\right) \mathbf{u}^{n+1} = \frac{1}{\nu} \left(\frac{\gamma_0}{\Delta t} \hat{\mathbf{u}} - \nabla p^{n+1}\right). \quad (2.6)$$

Here \mathbf{u}^n denotes the velocity vector evaluated at time $t = n\Delta t$, for $n \in \mathbb{N}$. The temporal accuracy is determined by the parameter J , which we fix to $J = 2$ in this work; i.e. $\gamma_0 = 3/2$, $\alpha_0 = 2$, $\alpha_1 = -1/2$, $\beta_0 = 2$ and $\beta_1 = -1$, but may be increased to 3 in Semtex.

The Poisson equation Eq. (2.5) must be equipped with a suitable Neumann boundary condition at inlet and walls [32]

$$\frac{\partial p^{n+1}}{\partial \mathbf{n}} = -\mathbf{n} \cdot \frac{\partial \mathbf{u}^{n+1}}{\partial t} - \mathbf{n} \cdot \sum_{q=0}^{J-1} \beta_q (\mathbf{N}(\mathbf{u}^{n-q}) + \mathbf{f}^{n-q} + \nu \nabla \times \boldsymbol{\omega}^{n-q}) \quad (2.7)$$

where $\boldsymbol{\omega} = \nabla \times \mathbf{u}$ is the vorticity. In summary, the NS momentum equation Eq. (2.3) can be solved efficiently using four sequential

steps Eqs. (2.4–2.6). Further details may be found in [5], and references therein.

We perform a high-order conformal Galerkin discretisation on the x - y or R - θ plane and couple the resulting scheme with a Fourier discretisation to account for the homogeneous streamwise z -direction. A complete discussion of the numerical methods for DNS is included in [5]. In the next section, we will introduce the necessary modifications to include the SVM, which will require the modification of the forcing term in Eqs. (2.1) and (2.3).

2.2. Explicit LES: Stretched-vortex model (SVM) adapted to a high-order h/p solver

We summarise here the main ingredients of Chung & Pullin's stretched-vortex model and detail the implementation in `Semtex`.

We start by considering the decomposition $u_i(t) = \tilde{u}_i(t) + u'_i(t)$, where the full-scale velocity $u_i(t)$ is decomposed into a filtered resolved-scale velocity $\tilde{u}_i(t)$ and an under-resolved velocity $u'_i(t)$ (and similarly for the pressure). Note that we have considered an implicit filtering, with the only filtering parameter being the cutoff length associated with the local grid-scale Δ_c (to be defined later). Introducing the decomposition into the NS equations, Eq. (2.1), we obtain

$$\frac{\partial \tilde{\mathbf{u}}}{\partial t} + \nabla \cdot (\tilde{\mathbf{u}} \otimes \tilde{\mathbf{u}}) = -\nabla \tilde{p} + \nu \nabla^2 \tilde{\mathbf{u}} - \nabla \cdot \mathbf{T}; \quad \nabla \cdot \tilde{\mathbf{u}} = 0, \quad (2.8)$$

where the stress tensor $T_{ij} = \tilde{u}_i \tilde{u}_j - \tilde{u}_i' \tilde{u}_j' = \tilde{u}_i \tilde{u}_j + u'_i u'_j + u'_i u'_j$, requires modelling.

The SVM [14,45], also called stretched-vortex model, is a structural subgrid model designed to represent the statistical effect of subgrid motion by using information from resolved scale quantities [45]. It is assumed that the subgrid vorticity in each cell comprises a superposition of stretched vortices, each unidirectional and of "cylindrical" type. Upon coordinate transformation from the vortex-fixed frame to the lab-fixed frame, the distribution of orientations of the vortex structures forms a probability density function (PDF), which reflects the local anisotropy of turbulence [52]. Extending the assumption that the ensemble dynamics of subgrid scale motions are dominated by a vortex aligned with a unit vector e_v (modelled via a delta-function PDF), the subgrid stress tensor is given by:

$$T_{ij} = (\delta_{ij} - e_i^v e_j^v) K. \quad (2.9)$$

This stress tensor \mathbf{T} , Eq. (2.9), is expressed in terms of the unit vector, e^v , and the subgrid kinetic energy K , which is given by the integral of the subgrid stress energy spectrum $E(k)$ as $K = \int_{k_c}^{\infty} E(k) dk$, where $k_c = \pi/\Delta_c$ is the cut-off wave number. The energy spectrum for turbulent incompressible flows $E(k)$ is known to have the asymptotic solution of the form of Eq. (2.10) for large wave number k , where ε is the dissipation rate per unit mass and η is the Kolmogorov length. This relation was initially obtained using dimensional reasoning by Kolmogorov, and later derived from the NS equations by Lundgren [40] for stretched spiral type vortices,

$$E(k) = \varepsilon^{2/3} k^{-5/3} F(\eta k) = \kappa_0 \varepsilon^{2/3} k^{-5/3} \exp\left(-\frac{2k^2 \nu}{3|\bar{a}|}\right), \quad (2.10)$$

where $\bar{a} = e_i^v e_j^v S_{ij}$ is the stretching along the subgrid vortex axis exerted by the resolved scales, and S_{ij} is the resolved strain-rate tensor. Upon integration of Eq. (2.10), with respect to k , the subgrid kinetic energy is obtained in terms of a group constant K'_0 and an incomplete gamma function:

$$K = \frac{1}{2} K'_0 \Gamma\left[-\frac{1}{3}, \kappa_c^2\right],$$

where $\Gamma[s, t] = \int_t^{\infty} u^{s-1} \exp(-u) du$. Here, $K'_0 = K_0 \varepsilon^{2/3} \lambda_\nu^{2/3}$, $\lambda_\nu = (2\nu/3|\bar{a}|)^{1/2}$ and $\kappa_c = k_c \lambda_\nu$. The approximation of $\Gamma[s, t]$ and the evaluation of K'_0 are given in [14].

The definition of the cut off length Δ_c is based on the Gauss-Lobatto points associated to the polynomial order in the high-order continuous-Galerkin discretisation, such that $\Delta_c = [\Delta_x \Delta_y \Delta_z]^{1/3}$. Instead of calculating neighbouring points in the Cartesian global system (x, y, z) , they are evaluated in the local (i, j, k) coordinate system of each element, such that: $\Delta_{c,ijk} = (l_{i+1} l_{i-1} l_{j+1} l_{j-1} l_{k+1} l_{k-1})^{1/6}$ where

$$\begin{aligned} l_{i+1} &= ((x_{i+1,jk} - x_{ijk})(y_{i+1,jk} - y_{ijk})(z_{i+1,jk} - z_{c,ijk}))^{1/3}, \\ l_{j+1} &= ((x_{i,j+1,k} - x_{ijk})(y_{i,j+1,k} - y_{ijk})(z_{i,j+1,k} - z_{ijk}))^{1/3}, \\ l_{k+1} &= ((x_{i,j,k+1} - x_{ijk})(y_{i,j,k+1} - y_{ijk})(z_{i,j,k+1} - z_{ijk}))^{1/3}, \end{aligned} \quad (2.11)$$

where l denotes the local coordinates. Note that this calculation is performed only once before the simulation begins, therefore causing little computation overhead. To clarify the notation and coordinate axis, we include Fig. 1, where the cylindrical coordinates and the local system based on Gauss-Lobatto points, used to define the subgrid cut-off length, are depicted.

Additionally, we have tested alternatives to this definition for the cut off length Δ_c . Instead of using Gauss-Lobatto points, one may consider a definition based on the polynomial expansion on the R - θ plane and distinguish the Fourier z -direction, e.g. $\Delta_c = [\Delta_{R-\theta} \Delta_z]^{1/3} = [A(\pi/P)^2 \Delta_z]^{1/3}$. The last expression is inspired by [29,31], where A defines the element area in 2D (i.e. the R - θ Galerkin plane), P is the polynomial order of the elements. The ratio π/k represents the resolved half wavenumber for a given polynomial of order P , see [29,31] and references therein. The simulated statistics obtained when using this last expression were very similar to those found when using Gauss-Lobatto points, Eq. (2.11), and therefore only Gauss-Lobatto results are included hereafter.

Finally, to implement the turbulence model into the splitting scheme in `Semtex` (see Section 2.1), we can redefine, in Eq. (2.3), $\mathbf{u} \rightarrow \tilde{\mathbf{u}}$ and $p \rightarrow \tilde{p}$ as the filtered large scale velocities and pressures. At each time step the divergence of subgrid stress matrix $\nabla \cdot \mathbf{T}$ is computed (see Eq. (2.9)) and incorporated to the temporal scheme through the forcing term \mathbf{f} , see Eq. (2.3). We treat this tensor explicitly in time, such that only the non-linear step in the splitting scheme, Eq. (2.4), requires modification by setting $\mathbf{f} = \nabla \cdot \mathbf{T}$.

2.3. Implicit LES: Spectral vanishing viscosity (SVV)

The main idea behind the spectral vanishing viscosity (SVV) technique is to add controlled artificial viscosity only to the highest modes in order to provide stabilisation in high order numerical methods. This technique does not modify the lowest modes and hence preserves the spectral accuracy of the method (see [49] or [34] for a detailed explanation). The SVV technique was originally conceived by Tadmor [61] to regularise the solution (i.e. avoid oscillatory phenomena) in the inviscid Burgers equation:

$$\frac{\partial}{\partial t} u(x, t) + \frac{\partial}{\partial x} \left[\frac{u^2(x, t)}{2} \right] = 0, \quad (2.12)$$

subject to appropriate initial and boundary conditions. Tadmor introduced in Eq. (2.12) a convolution term that only acts on high wavenumbers, leaving low wavenumbers unchanged. The discrete form of the previous Burgers equation with the regularisation term reads:

$$\frac{\partial}{\partial t} u_N(x, t) + \frac{\partial}{\partial x} \left[\mathcal{P}_N \left(\frac{u^2(x, t)}{2} \right) \right] = \epsilon \frac{\partial}{\partial x} \left[Q_N * \frac{\partial u_N(x, t)}{\partial x} \right], \quad (2.13)$$

where $u_N(x, t)$ is the N th order modal approximation of $u(x, t)$, \mathcal{P}_N is a projection operator and $*$ represents the convolution. In addition, Q_N is a damping function (also called *viscosity kernel*) that becomes active for high wavenumbers only. In the particular case

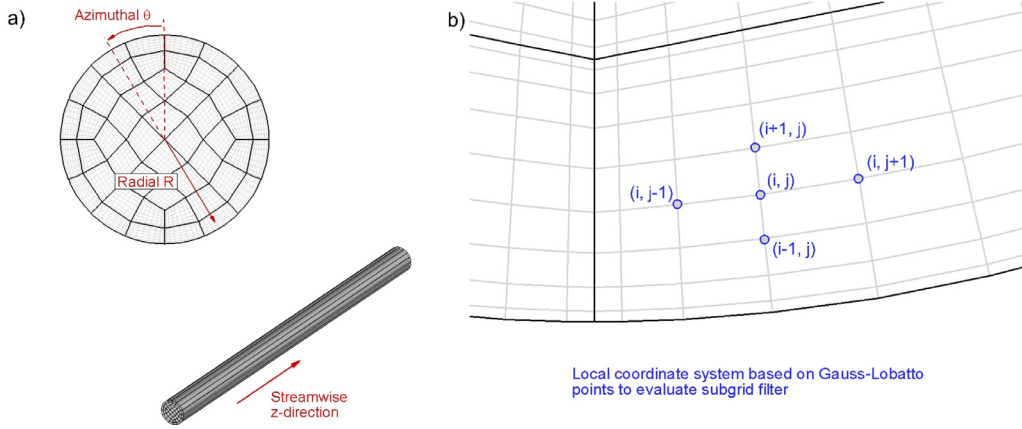


Fig. 1. a) Cylindrical coordinates for pipe simulations and b) detailed view of one spectral element. The local coordinate system (i, j) and Gauss-Lobatto points used to define the cut-off length are included in the figure.

of a Fourier discretisation (i.e. the streamwise z -direction in this work), the SVV regularisation term becomes:

$$\epsilon \frac{\partial}{\partial x} \left[Q_N * \frac{\partial u_N(x, t)}{\partial x} \right] = -\epsilon \sum_{P_{cut} \leq |k| \leq N} k^2 \tilde{Q}_k \tilde{u}_k e^{ikx}, \quad (2.14)$$

where k is the wave number, N is the number of Fourier modes and P_{cut} is the wavenumber for the damping function to become active. Various definitions for the Kernel \tilde{Q}_k have been proposed (e.g. Tadmor [61]) but in this work, we retain the formulation of Maday [41] and Xu and Pasquetti [64]:

$$\tilde{Q}_k = \exp \left[-\frac{(k-N)^2}{(k-P_{cut})^2} \right], \quad k > P_{cut}. \quad (2.15)$$

Note that it is necessary to define the cut-off wavenumber P_{cut} and the spectral viscosity ϵ . As in Xu and Pasquetti [64] or Koal et al. [37], the present implementation uses: $P_{cut} = N/2$ and $\epsilon = \epsilon_{SVV} \nu$, where ϵ is proportional to the kinematic viscosity ν and ϵ_{SVV} is a constant that controls the amount of SVV viscosity.

In the $R-\theta$ plane, quadrilateral nodal spectral elements are used to discretise the pipe. When using two-dimensional tensor products of one-dimensional Lagrange interpolants through the Gauss-Lobatto quadrature points, the derivative operator matrices that construct the diffusion operators are modified via: (i) Transformation to Legendre polynomial space; (ii) factorization with a diagonal matrix of form: $\text{diag}[1 + (\epsilon/\nu)\tilde{Q}_k]^{1/2}$, where \tilde{Q}_k is of the same form as when considering the Fourier direction, but where now N is the order of the Gauss-Lobatto Lagrange interpolants ($N=9$ in this work) and k is a Legendre polynomial index; and (iii) inverse transformation from Legendre polynomial space to physical space. Refer to [37] for further details.

As mentioned, the SVV method requires adjustment of the cut-off wavenumber P_{cut} and the spectral viscosity ϵ . Various studies have attempted to derive parameter-free SVV techniques, where these parameters are computed using different ideas. For example, Karamanos and Karniadakis [30], Kirby and Karniadakis [35] or more recently or Manzanero et al. [42] have computed the amount of SVV viscosity using a Smagorinsky model. Additionally, Moura et al. [30] and also Manzanero et al. [42] analyse the numerical errors of continuous and discontinuous Galerkin schemes (based on Von Neumann analyses) to set the cut-off wavenumber P_{cut} . Despite these efforts and to the authors's knowledge, there are no universal parameter-free SVV schemes usable for all Reynolds numbers and flow conditions, and hence these parameters will be calibrated in upcoming sections, as in [37,49].

2.4. Wall modelling: The virtual-wall model (VWM)

A major challenge for LES of wall-bounded flows is that the turbulent length scales become progressively smaller towards the wall due to confinement of the near-wall eddies. In near wall resolved LES, this is addressed by introducing a very fine uniform mesh near walls. This enables the capture of near-wall fine scales but requires a very high computational effort. In wall-modelled LES methods (WMLES), near-wall fine scales are modelled, thus eliminating the need for very fine meshes.

Recent reviews of wall models for LES have been compiled by Larsson et al. [38] and Bose and Park [7], and update classic reviews [51,60]. Larsson et al. explain that WMLES methods may be categorised in two approaches: hybrid LES/RANS methods and wall-stress models. The former utilises Reynolds Averaged Navier-Stokes (RANS) to model the turbulent behaviour near walls, while the latter type develops wall-stress models to avoid resolving the near-wall region. Additionally, Larsson et al. detail that a drawback of the hybrid LES/RANS methods is that an ‘‘artificial buffer layer’’ with log-layer mismatch may occur leading to artificial physical structures that survive into the LES region. Physics-based wall-stress models do not show artificial layers and have seen increasing popularity during the last decade. The underlying idea of wall-stress models is that an estimate of the instantaneous wall shear stress vector can be obtained given an instantaneous velocity at a certain distance above the wall. Note that to avoid resolving turbulence in the near-wall region, the wall-model equations must be expressed as low-pass filtered or ensemble-averaged. In this work we employ the ensemble-averaged approach.

Wall-stress models can be formulated from the filtered form Eq. (2.8), introducing boundary layer approximations (considering x , y and z , the spanwise, wall-normal and streamwise directions), to obtain the following ODE:

$$\frac{\partial \tilde{u}}{\partial t} + \frac{\partial \tilde{u} \tilde{u}}{\partial x} + \frac{\partial \tilde{u} \tilde{v}}{\partial y} + \frac{\partial \tilde{u} \tilde{w}}{\partial z} = -\frac{\partial \tilde{p}}{\partial x} + \nu \frac{\partial^2 \tilde{u}}{\partial y^2}. \quad (2.16)$$

From Eq. (2.16) and assuming exact balance between convection and the pressure-gradients, one may obtain the simplest wall model: the well known law of the wall where $u^+ \approx y^+$ for $y^+ \lesssim 5$ and $u^+ \approx \ln(y^+)/\kappa + C$ for $y^+ \gtrsim 30$. Other simple models are reviewed in [51,60].

In this work, we employ the *virtual-wall model* (VWM) proposed by Chung and Pullin [14], where an ODE is derived to model the time variation of instantaneous, filtered wall skin-friction velocity. The resulting ODE is driven by a forcing term that depends on the resolved scales at a distance h from the wall. This distance h is generally smaller than the first wall adjacent mesh element, and

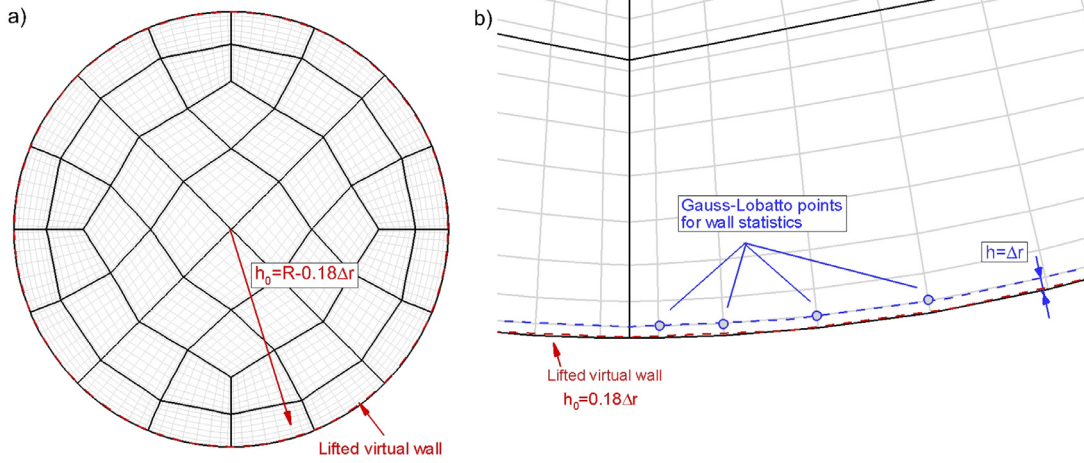


Fig. 2. Sketched of mesh including the location of the virtual-wall model: a) Shows the virtual wall location with respect to the pipe and b) Provides a detailed view of a cell element. The statistics for the model are collected at Gauss–Lobatto points, which are close to the height h_0 . The wall cell height h and the virtual wall location $h_0 = 0.18h$ are included in the figure.

in our high-order implementation corresponds to the first Gauss–Lobatto point (closest to the wall), see Fig. 2 for an illustration. The VWM has been validated for LES of smooth and rough-wall channel flows [56,57] and for fully developed turbulent boundary-layer flow for both zero pressure gradient [26,27] and attached-flow APG cases [28].

More precisely, Chung and Pullin argued in [14] that the dominant parameter for near wall-modelling is u_τ , which can be calculated by averaging Eq. (2.16) in the wall-normal direction and relying in local inner scaling to treat the time-dependence of the filtered wall-parallel velocity. Consequently the notation used here is particularised to the expectation that the basic flow (and slip velocity) is aligned with the streamwise z -direction. The resulting ODE describes the local wall-normal velocity gradient $\eta_0 = \partial \tilde{u} / \partial y$ or equivalently $u_\tau^2 = \nu \eta_0$. At the interface between the wall model and outer flow region, Chung & Pullin define a slip velocity, thus providing the outer LES with slip Dirichlet boundary conditions; i.e. at a lifted virtual wall.

In this work, the streamwise, wall-normal, and spanwise directions are set as x ; y ; z directions; the adaptation to cylindrical pipe coordinates will be introduced later for simplicity. As in SVM, we introduce an ODE for the wall-normal shear stress at the wall:

$$\frac{\tilde{u}|_h}{2\eta_0} \frac{\partial \eta_0}{\partial t} + \frac{\partial \langle \tilde{u} \tilde{u} \rangle}{\partial x} + \frac{\partial \langle \tilde{u} \tilde{w} \rangle}{\partial z} + \frac{1}{h} \tilde{u} \tilde{w} \Big|_h = - \frac{\partial \tilde{p}}{\partial x} \Big|_h + \frac{\nu}{h} \left(\frac{\partial \tilde{u}}{\partial y} \Big|_h - \eta_0 \right), \quad (2.17)$$

$$\tilde{u}|_{h_0} = u_\tau \left(\frac{1}{\kappa} \log(h_0^+ + B) \right) \quad (2.18)$$

with $u_\tau^2 = \nu \eta_0$. Here $\langle \tilde{\phi}(x, z, t) \rangle = h^{-1} \int \tilde{\phi}(x, y, z, t) dy$ denotes the spatial average in the wall normal direction, see further details in [14]. Note that in our notation z denotes the streamwise component and not x as in [14]. Let us note that the Kármán-like parameter κ in Eq. (2.18) is not chosen a priori but evaluated dynamically during the course of the simulations. Eq. (2.18) may be rewritten as

$$\frac{d\eta_0}{dt} = \Lambda(t) \eta_0 (\gamma - \eta_0), \quad (2.19)$$

where $\Lambda(t)$ and $\gamma(t)$ are defined as

$$\Lambda(t) = \frac{2\nu}{h w|_h}; \quad \gamma(t) = - \frac{h}{\nu} \left(\frac{\partial \langle \tilde{u} \tilde{u} \rangle}{\partial x} + \frac{\partial \langle \tilde{u} \tilde{w} \rangle}{\partial z} + \frac{1}{h} \tilde{u} \tilde{w} \Big|_h + \frac{\partial \tilde{p}}{\partial x} \Big|_h \right) - \frac{\partial \tilde{u}}{\partial y} \Big|_h, \quad (2.20)$$

The formal analytic solution to Eq. (2.19) may be found in [14]:

$$\frac{1}{\eta_0(t)} = \frac{1}{\eta_0(0)} + I(t) \int_0^t \frac{\Lambda(s)}{I(s)} ds, \quad (2.21)$$

and

$$I(t) = \exp \left(\int_0^t \Lambda(s) \gamma(s) ds \right). \quad (2.22)$$

For the purposes of solving the ODE, the function $\Lambda(t)$ and $\gamma(t)$ can be considered functions of time sourced from information supplied by the LES at $y = h$. Eq. (2.21) is approximated to first order to obtain Eq. (2.23) in our implementation

$$\frac{1}{\eta_0(t)} = \frac{1}{\eta_0(0)} \exp(-t \Lambda(0) \gamma(0)) - \frac{1}{\gamma(0)} (1 - \exp(-t \Lambda(0) \gamma(0))). \quad (2.23)$$

We adapt the ODE Eq. (2.20) to cylindrical coordinates, such that x – y represents the cross-section of the circular pipe, with radius R and azimuthal angle θ and z runs along the longitudinal streamwise direction, see Fig. 1, to obtain:

$$\Lambda(t) = \frac{2\nu}{h w|_{R-h}}; \quad \gamma(t) = - \frac{h}{\nu} \left(\frac{\partial \langle \tilde{w} \tilde{w} \rangle}{\partial z} + \frac{1}{R} \frac{\partial \langle \tilde{w} \tilde{u}_\theta \rangle}{\partial \theta} + \left(\frac{1}{R} - \frac{1}{h} \right) \tilde{w} u_r \Big|_{R-h} + \frac{\partial \tilde{p}}{\partial z} \Big|_{R-h} \right) - \frac{\partial \tilde{w}}{\partial r} \Big|_{R-h} - \frac{\tilde{w}|_{R-h}}{R}, \quad (2.24)$$

where u_r and u_θ denote the radial and azimuthal flow directions. The slip velocity is calculated locally and dynamically through $u_\tau^2 = \nu \eta_0$ (where η_0 is obtained by solving Eq. (2.21)), which requires the ability to apply the time- and space-varying Dirichlet boundary conditions. It has been found that the wall-normal velocity (even when considering roughness [57]) is three to four orders of magnitude smaller than the wall-parallel slip velocity; thus, the vertical velocity at the virtual wall is omitted in our simulations.

Finally, as proposed in [14,27,56,57], the spatially averaged terms, in Eq. (2.24), can be approximated by sampling resolved and

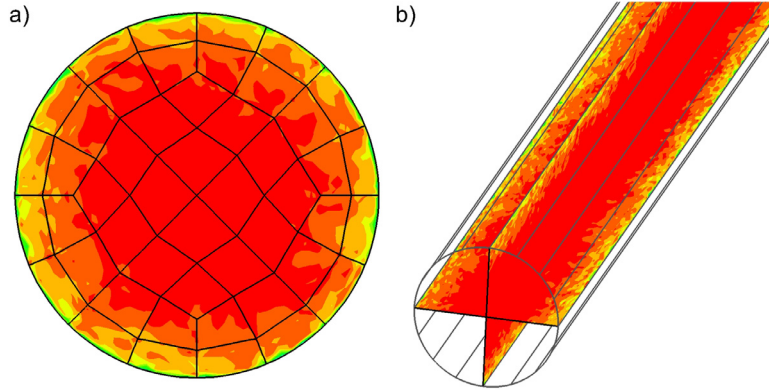


Fig. 3. SVM at $Re_\tau = 1.8 \times 10^5$: a) Flow solution isocontours of streamwise velocity at a) sectional pipe ($R-\theta$) plane and b) longitudinal planes ($R-z$) along the pipe; a) and b) show 11 contours ranging from 0 to 1.

modelled quantities (when available); for example, using the approximation:

$$\frac{\partial \langle \tilde{u}_i \tilde{u}_j \rangle}{\partial x_j} \approx \frac{\partial \tilde{u}_i \tilde{u}_j |_h}{\partial x_j} = \frac{\partial \tilde{u}_i |_h \tilde{u}_j |_h}{\partial x_j} + \frac{\partial T_{ij}}{\partial x_j |_h}. \quad (2.25)$$

Note that when subgrid scales are modelled (as in the stretched vortex SGS model), we typically use the right hand side of Eq. (2.25) and compute the subgrid terms using Eq. (2.9). However, when using implicit LES (see Section 2.3), these subgrid terms are not modelled and are not available. One possibility to close the wall model is to use the definition of T_{ij} from the stretched vortex SGS model, even when the model is not active (in the momentum equation Eq. (2.8)). A second option is to approximate $\langle \tilde{u}_i \tilde{u}_j \rangle \approx \tilde{u}_i |_h \tilde{u}_j |_h$ and neglect under-resolved fluctuations close to the wall such that $T_{ij} = 0$. We use the last option, which is less costly, after having tested both possibilities and observing only minor differences.

2.4.1. Summary of the virtual-wall model

Three main steps are required to compute the slip boundary condition for LES:

1. The friction velocity u_τ is calculated locally and dynamically over the time-step, making use of the relation $u_\tau^2 = \nu \eta_0$, where η_0 is obtained by solving Eq. (2.21). The input to the analytic function, Eq. (2.21), is supplied by the outer LES (at distance h from walls).
2. With an updated u_τ , now known at every point on the wall, a local slip velocity is calculated using Eq. (2.24) and is supplied to the outer LES as the boundary conditions at the lifted virtual wall (at distance h_0).
3. With the boundary condition at each grid point on the virtual wall now known, one time-step of the LES equations is then performed using `Semtex`, Eq. (2.3).

In terms of assumptions, inputs and interactions, we can summarize the framework as follows. The VWM assumes inner-scaling in calculating the friction velocity and slip velocity; it is in this way that the wall model is designed to be optimal for high Reynolds number flow, where such scaling is clearly identified. Operating on smooth walls, the model requires two empirical values: the log-linear profile intersect, h_v^+ and virtual wall height, $h_0 = 0.18h$, where $h = \Delta r$ is the height of the first wall-adjacent cell. We have not found noticeable differences when varying h_0 , which is consistent with the numerical tests of SVM [14]. To clarify the notation introduced in this last section, we provide a sketch of mesh, in Fig. 2, and include the height of the first mesh element h (adjacent to the wall) where the statistics necessary for the wall model

are collected. Additionally, at height $h_0 = 0.18h$, we depict the location of the lifted virtual wall (almost overlapped to the physical wall). In practice, since the solver has a nodal structure, the statistics are collected at the first Gauss-Lobatto points at the edge of the first cell (at a distance h).

2.5. Mesh resolution and post-processing

The computational domain is set to have dimensions ($R; \theta; l_z$) = (0.5; 2π ; $2\pi/0.4 \sim 15.7$) and uses approximately 1.5 M node points. Using a cylindrical formulation, we take the streamwise z -direction as the Fourier direction and use 320 z -planes. Each plane consists of 48 elements, as shown in Figs. 1–3. Elements are organized into four layers in the radial R -direction, with the two outer-most layers having 16 elements around the circumferential θ -direction. Along with the 320 z -planes and 9th order polynomials ($P=9$), we aim to have an effective grid size ratio of $dr : dz = 1 : 4$, based on our previous experience [14,45,57] in using the SVM. We use the same mesh for explicit and implicit LES computations.

The Reynolds numbers selected for the simulations are chosen based on the existence of available experimental data. These Reynolds numbers based on the pipe radius and friction velocity are varied from $Re_\tau = 2 \times 10^3$ to $Re_\tau = 1.8 \times 10^5$. Defining the $Re_D = u_b D / \nu$, where u_b is the bulk velocity and D denotes the pipe diameter. The corresponding bulk Reynolds numbers are $Re_D = 9.18 \times 10^4$ and 1.65×10^8 , respectively, according to Blasius' correlation. In this work, the mesh does not change with Reynolds number, and hence increasing Reynolds number corresponds to increasing under-resolution. Taking the first inner Gauss-Lobatto point as reference length (see Fig. 2), we compute the non-dimensional mesh sizes of $(\Delta r^+ = \Delta y^+; \Delta \theta^+; \Delta z^+) = (12.1; 31.6; 196.4)$ and $(\Delta r^+ = \Delta y^+; \Delta \theta^+; \Delta z^+) = (1208.5; 3163.7; 19667.8)$ for the low and high Reynolds numbers, respectively. The mesh and instantaneous stream-wise velocity are shown in Fig. 3 for Reynolds number $Re_\tau = 1.8 \times 10^5$.

To compute flow statistics, raw data is first averaged over the stream-wise direction (Fourier direction). Then, the stream-wise-averaged data is sampled at forty evenly spaced points, defined radially from the pipe center to the virtual wall. Should one of these sample points not coincide with a knot point of the Gauss-Lobatto-Legendre basis functions, a two-dimensional interpolation is carried out. This sample is referred to as a “ray”. Sixteen of such rays are sampled around the circumferential direction with equal angular spacing, and subsequently averaged to obtain the final profiles.

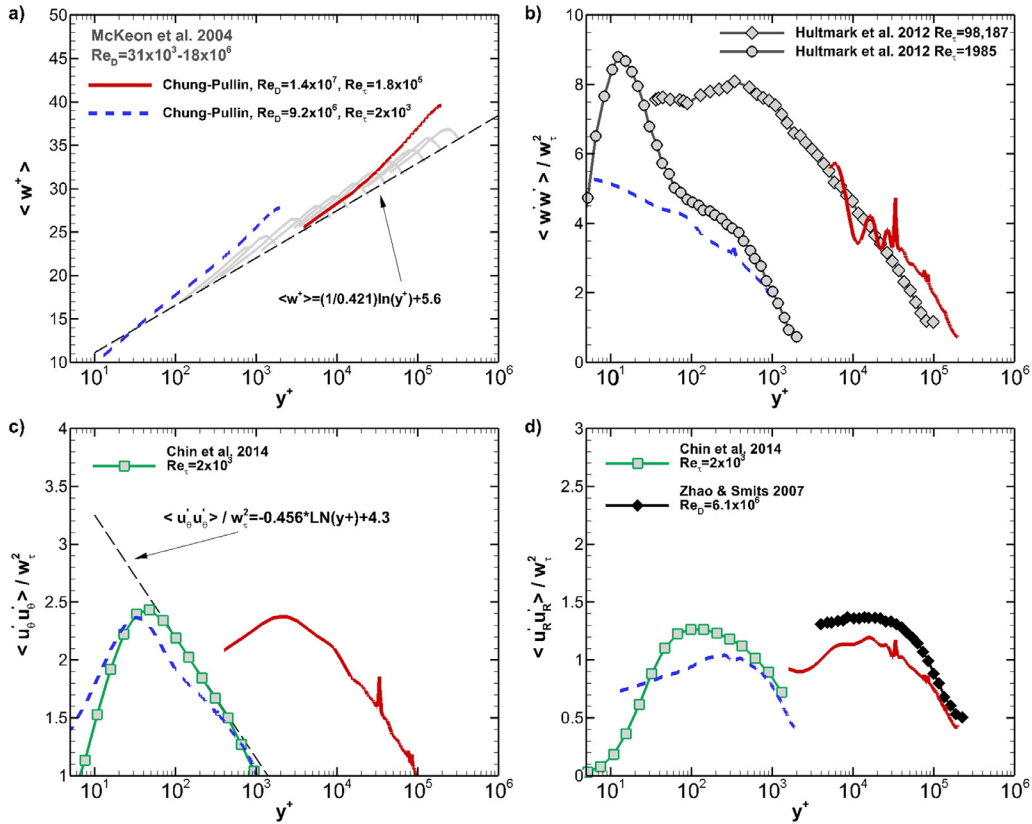


Fig. 4. Chung & Pullin model (SVM): Comparison of turbulence statistics for pipe flow at $Re_\tau = 2 \times 10^3$ and 1.8×10^5 ; a) mean streamwise velocity; b), c) and d) streamwise, azimuthal and radial Reynolds stresses, respectively.

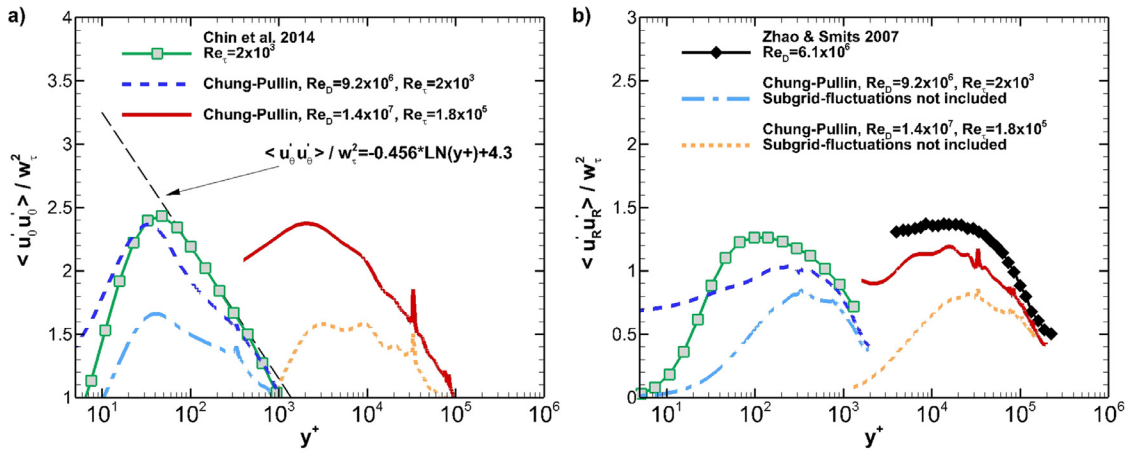


Fig. 5. Chung & Pullin model (SVM): Comparison of turbulence statistics for pipe flow at $Re_\tau = 2 \times 10^3$ and 1.8×10^5 . Effect of including subgrid fluctuations in (a) azimuthal and (b) radial Reynolds stresses.

3. Results and discussion

Experimental data used for comparison in following sections has been extracted from published work. McKeon et al. [43] supplied mean streamwise data for a large range of Reynolds number $Re_D = 31 \times 10^3$ to 18×10^6 . Streamwise fluctuations are provided by Hultmark et al. 2012 [25] at $Re_\tau = 1985$ and 98187 . Azimuthal and radial Reynolds stresses are available at $Re_\tau = 2 \times 10^3$, from Chin et al. [11], and radial Reynolds stresses for $Re_D = 6.4 \times 10^6$ have been extracted from Zhao and Smits 2007 [66]. These experiments cover the two Reynolds numbers simulated in this work and enable comparison for streamwise, azimuthal and radial statistic.

Note that in what follows the radial distance to the wall is denoted Δy^+ . We present results for two relatively high Reynolds numbers $Re_\tau = 2 \times 10^3$ and 1.8×10^5 . First, we include results issued from the SVM. Second, we study the spectral vanishing viscosity results with and without wall models.

3.1. Explicit LES: Stretched-vortex model

Fig. 4 compares SVM to experimental data. We observe general agreement for both Reynolds numbers $Re_\tau = 2 \times 10^3$ and 1.8×10^5 . Additional Reynolds numbers may be found in the Ph.D. thesis of the second author [55]. The mean streamwise velocity distributions follow the log distribution and agree well with the experimental

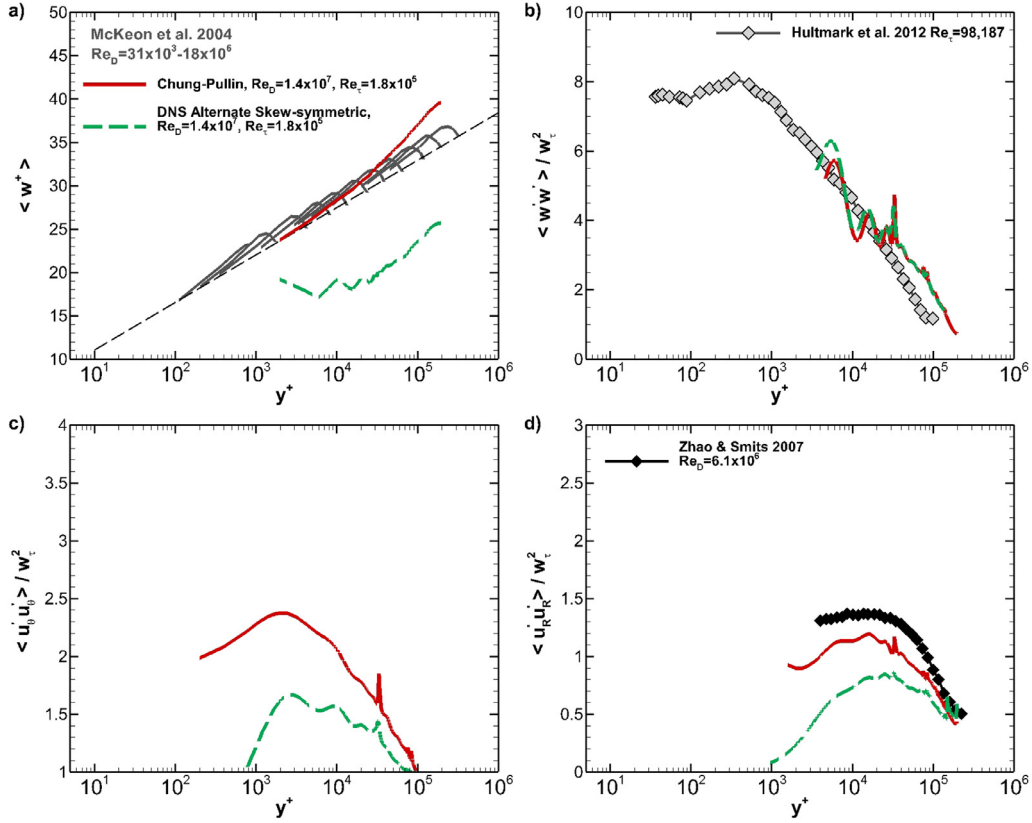


Fig. 6. No model: No explicit or implicit model is included. The simulation is stable when using the alternate skew-symmetric for $Re_\tau = 1.8 \times 10^5$; a) mean streamwise velocity; b), c) and d) streamwise, azimuthal and radial Reynolds stresses, respectively.

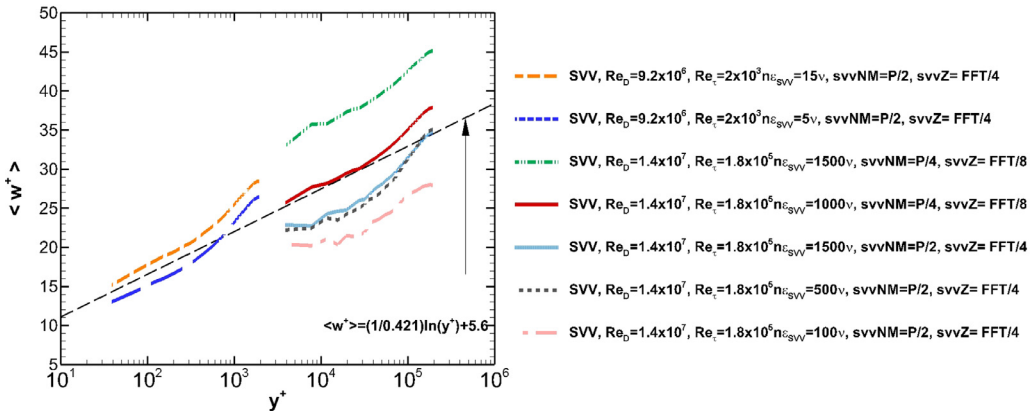


Fig. 7. SVV model: Comparison of turbulence statistics for pipe flow at $Re_\tau = 2 \times 10^3$ and 1.8×10^5 ; and calibration of SVV parameters.

data. The Reynolds stresses also agree remarkably well with experimental data. The stresses depicted in Fig. 4 include the subgrid contribution that are computed in a post-processing step and added to the solution (resolved-scales), following $\tilde{u}_i \tilde{u}_j = \tilde{u}_i \tilde{u}_j + T_{ij}$, see Eq. (2.8). These stresses follow the experimental data once the under-resolved fluctuations, are included into the resolved-scales. To discern the effect of the post-processing step, we depict in Fig. 5 the azimuthal and radial stresses with and without the subgrid contributions. It is noticeable that the resolved stresses curves are low compared to the experiments but once the subgrid correction are included, the results agree well with experiments. Let us note that including the under-resolved (or subgrid) contributions is only possible when using explicit subgrid models. This procedure will not be performed when using implicit LES using SVV, since the subgrid information is not available.

3.2. Implicit LES: SVV without wall model

Before activating the spectral vanishing viscosity model, we perform a preliminary simulation without any turbulence model at the highest Reynolds number $Re_\tau = 1.8 \times 10^5$. When using the alternate skew-symmetric form in the given grid, we find that the simulation is stable, which is a beneficial consequence of using a skew-symmetric form. Note that when using other forms to discretise the non-linear terms, e.g. convective form, the simulations were unstable.

The “no-model” result (using the alternative skew-symmetric form but without explicit or implicit subgrid modelling) is depicted in Fig. 6, together with the previous result using the SVM explicit model for comparison. It can be seen that when we do not include any model, the statistics are very different from the ex-

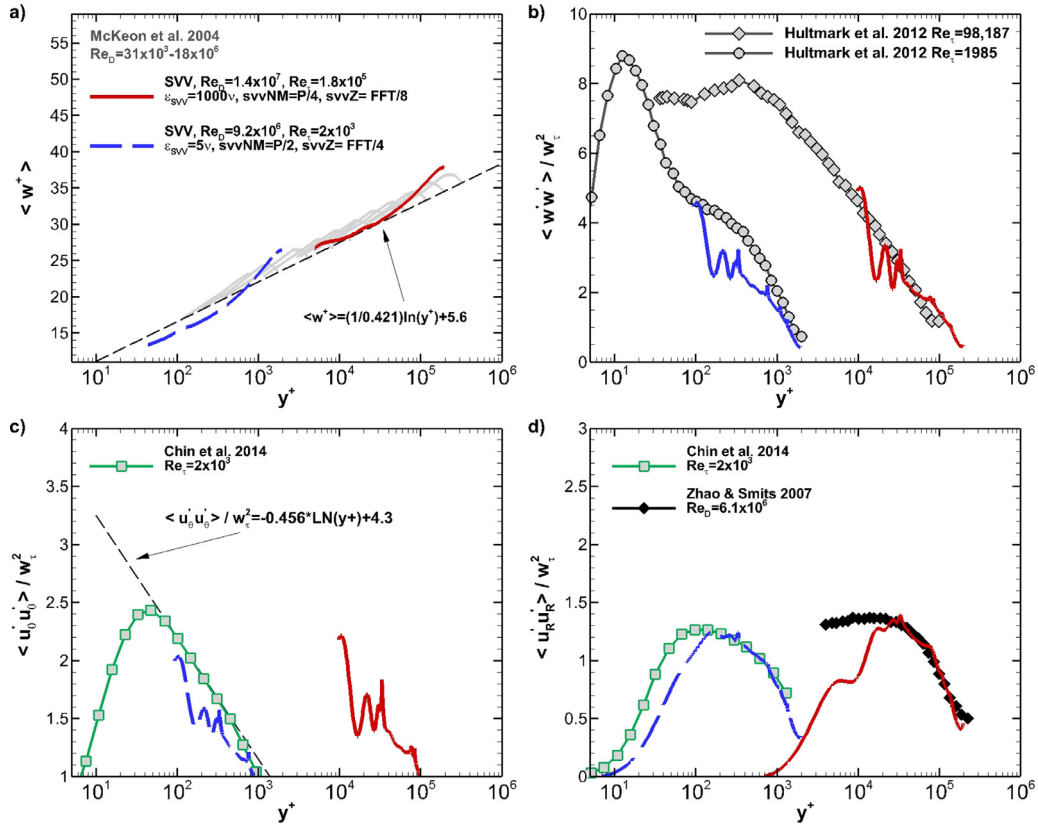


Fig. 8. SVV model: Comparison of turbulence statistics for pipe flow at $Re_\tau = 2 \times 10^3$ and 1.8×10^5 ; a) mean streamwise velocity; b), c) and d) streamwise, azimuthal and radial Reynolds stresses, respectively.

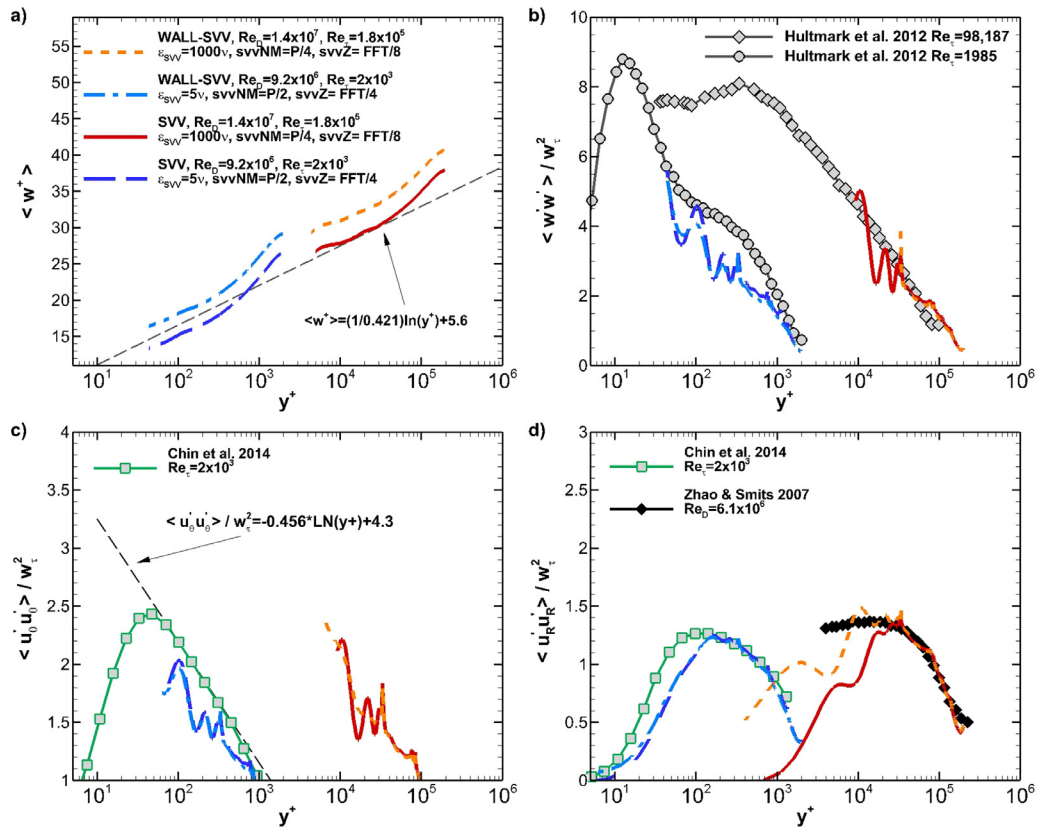


Fig. 9. WALL-SVV: Comparison of turbulence statistics for pipe flow at $Re_\tau = 2 \times 10^3$ and 1.8×10^5 ; a) mean streamwise velocity; b), c) and d) streamwise, azimuthal and radial Reynolds stresses, respectively.

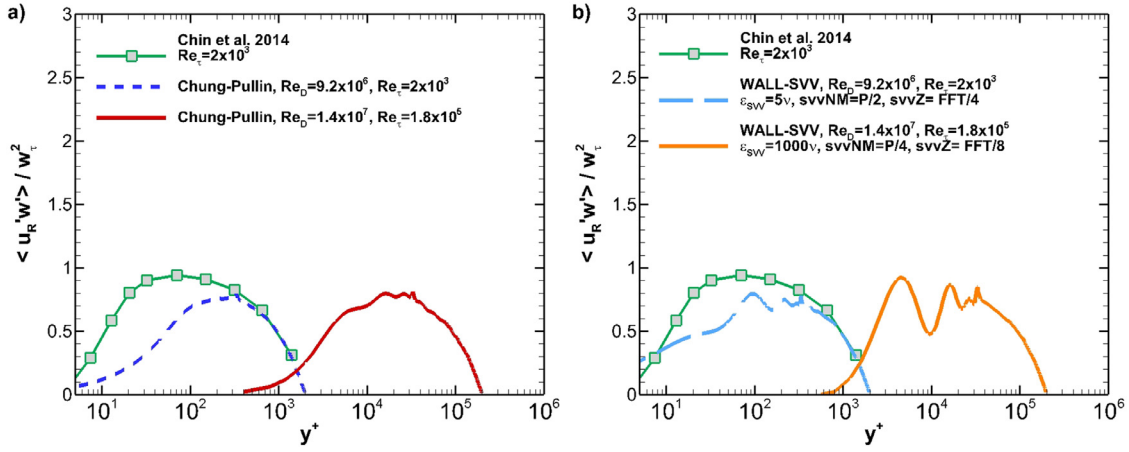


Fig. 10. Comparison of Reynolds shear stresses $\langle u_R'w' \rangle$ for pipe flow at $Re_\tau = 2 \times 10^3$ and 1.8×10^5 ; a) Chung & Pullin model (SVM) and b) WALL-SVV.

periments. These results may seem counter-intuitive since, when running implicit LES simulations, typically one may think that a stable solution with minimal numerical dissipation should provide the best result, but this is not the case. Here, the stable simulation with minimal numerical dissipation (i.e. “no-model” using the alternative skew-symmetric form) does not provide accurate results, which suggests that additional subgrid dissipation is necessary. Similar observations for turbulent flows using implicit LES methods with compressible discontinuous-Galerkin formulations (using skew-symmetric forms as stabilising mechanism) have been reported by Flad and Gassner [18]. Indeed, stable simulations do not guarantee accuracy in under-resolved turbulence, and additional dissipation is required to account for the missing physics of the subgrid scales.

We now simulate cases including the SVV model. The SVV method requires adjustment of two parameters: The SVV viscosity, ϵ_{SVV} , and cut-off wave-number, SVV_{NM} acting on $R - \theta$ planes and SVV_Z in the streamwise direction. These values are calibrated, for each Reynolds number, by adjusting the mean streamwise velocity to the log distribution. We illustrate the calibration of the SVV constants (without wall modelling) in Fig. 7. Note that only some selected simulations are retained here.

For the high Reynolds number, we observe, in Fig. 7, that the combination $\epsilon_{SVV} = 1000\nu$ with $SVV_{NM} = P/4$ and $SVV_Z = FFT/4$ provides good results. All the other curves are obtained by varying both the SVV viscosity or the cut-off wave-numbers and provide incorrect mean statistics. Additionally, for the low Reynolds number, we show the effect of varying ϵ_{SVV} from 5ν to 15ν (i.e. increased by a factor of 3). We observe a significant effect, which is comparable to keeping the SVV viscosity to 5ν and including wall modelling (see Section 3.3).

Once the mean is adjusted, no other tuning is necessary to obtain the depicted Reynolds stresses. Fig. 8 compares the implicit SVV model with experiments. We observe very good agreement for both Reynolds numbers and a clear improvement over the “no-model” method shown previously in Fig. 6. With the SVV method, the Reynolds stresses agree well with experiments. We remind the reader that despite that subgrid contributions cannot be included, in the post-processing step (when using implicit subgrid models) the curves match remarkably well with the experiments. This indicates that more scales are resolved when using the implicit model than when using the explicit SVM LES technique. Finally, let us note that some oscillations may appear near walls for the streamwise and azimuthal Reynolds stresses. If necessary, these oscillations can be damped by increasing the numerical damping through the parameter SVV_Z for the streamwise stresses and SVV_{NM} for the

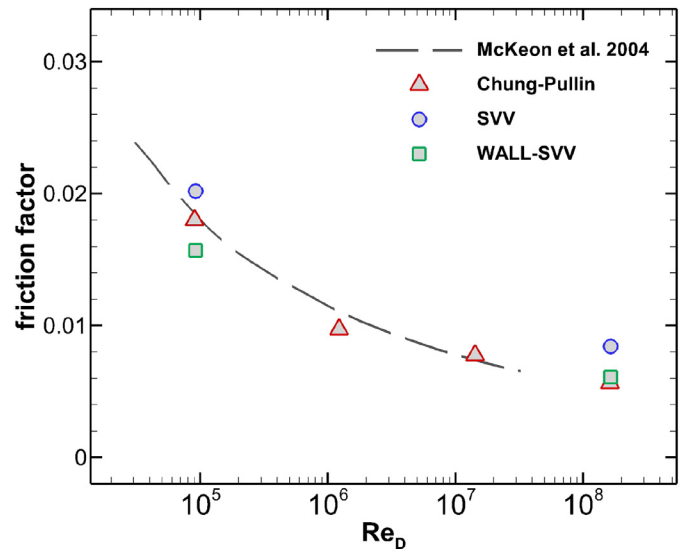


Fig. 11. Friction factor f with Reynolds number based on bulk velocity: Chung & Pullin model (SVM), SVV, WALL-SVV and experimental result of McKeon et al. [44].

azimuthal stresses. However, in our results we have preferred to minimise these values and allow for mild oscillations.

3.3. Implicit LES: SVV with wall model

In this section, we incorporate the virtual-wall model (VWM) to the implicit SVV simulations and compare the results to the previous SVV simulations without wall modelling. Fig. 9 shows comparisons for the SVV with and without wall modelling, labeled WALL-SVV and SVV, respectively. It can be seen that for fixed SVV parameters, both perform relatively well and that the SVV (without wall model) provides similar fluctuating quantities but higher mean streamwise distributions. Reynolds stresses are almost identical. For completeness, in Fig. 10 we compare the Reynolds shear stresses $\langle u_R'w' \rangle$ issued from the SVV with wall modelling to the SVM. We observe that both provide good results when compared to experimental data.

Additionally, we compute the friction factor

$$f = \frac{-\frac{dp}{dz} D}{\frac{1}{2} \rho W^2},$$

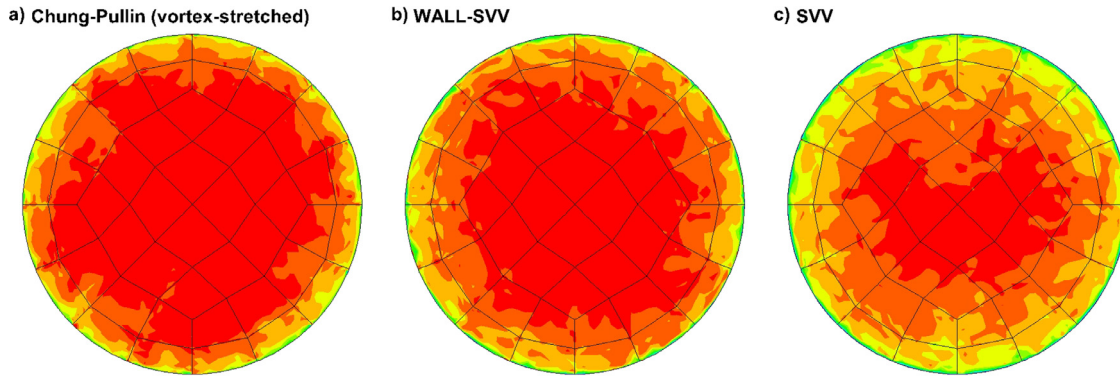


Fig. 12. Snapshots of streamwise velocity for pipe flow at $Re_\tau = 1.8 \times 10^5$; showing 11 contours ranging from 0 to 1.

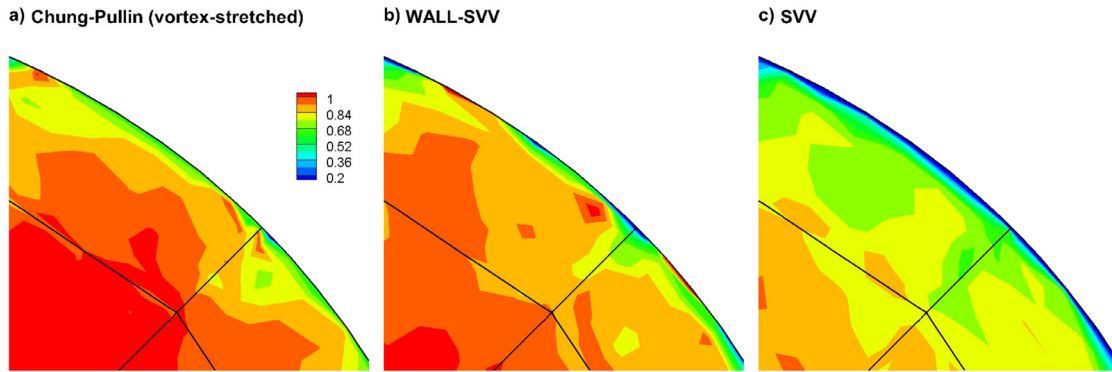


Fig. 13. Near wall snapshots of streamwise velocity for pipe flow at $Re_\tau = 1.8 \times 10^5$. Showing 11 contours ranging from 0.2 to 1.

where $\frac{dp}{dz}$ is the pressure drop per unit length, D is the diameter of the pipe, ρ is the fluid density and \bar{W} is the streamwise flow velocity averaged over the cross-sectional area of the pipe. We depict the results for the three LES models in Fig. 11 and observe reasonable agreement with the experimental results of McKeon et al. [44] and that the SVV without wall modelling over-estimates the friction factor, behaviour which is corrected when using wall modelling. Note that, for the Chung & Pullin model (SVM), two additional friction factors for Reynolds numbers $Re_\tau = 2 \times 10^6$ and 2×10^7 have been included in the figure. Details for these additional computations may be found in the PhD thesis of the second author [55].

Finally, to clarify the influence of wall modelling, we compare the instantaneous flow fields using the SVM explicit model and the SVV model without and with wall modelling, in Fig. 12. We observe that SVM (Fig. 12(a)) and WALL-SVV (Fig. 12(b)) provide very similar flow field distributions and comparable boundary layer thickness. However, the SVV without wall modelling (Fig. 12(c)) shows a thicker boundary layer, which translates into a lower mean streamwise curve in Fig. 9. To recover a similar velocity distribution, one should increase the SVV viscosity (ϵ_{SVV}) by a factor of 3 (see previous Fig. 8), which results in a more dissipative simulation. For completeness, we depict the near wall region for the same three cases in Fig. 13. Fig. 13(a) and (b) show a non-zero streamwise velocity at the slip wall, when using near-wall modelling, while zero velocity at walls is observed when using the SVV model without wall modelling, Fig. 13(c). These last figures show how the use of high-order polynomials (e.g. $P = 9$ here) helps resolving turbulent features even when selecting very coarse mesh elements.

We have observed that including a wall model when computing implicit LES, has limited influence in the Reynolds stresses but noticeable variations in the mean streamwise velocity. These results

suggest that wall models help to distinguish between the bulk dissipation and near wall dissipation and that these do not necessary need to be similar. Finally, including the wall model, when using implicit LES, enables lower artificial SVV viscosity, hence providing accurate results with diminished dissipation (when compared to implicit simulations without wall models).

4. Conclusions

We have introduced explicit and implicit large eddy simulation techniques in the high-order h/p spectral solver *Semtex* to compute fully developed turbulent pipe flows at two Reynolds numbers $Re_\tau = 2 \times 10^3$ and $Re_\tau = 1.8 \times 10^5$. Both methods, stretched-vortex model (SVM) by Chung & Pullin and the spectral vanishing viscosity (SVV) provide accurate statistics at both Reynolds numbers considered. Particularities of each model are summarised here:

- To retrieve the Reynolds stresses accurately the explicit LES method requires the inclusion of the under-resolved subgrid fluctuations, retrieved from the explicit subgrid model (see Section 3.1), which is performed in a post-processing step.
- The implicit SVV method provided accurate results for the Reynolds stresses even if its implicit nature does not provide access to the subgrid stresses (which cannot be included a posteriori).
- The implicit SVV method requires calibration of the SVV constants, which in this work is performed by matching the mean-streamwise velocity. The Reynolds stress values were not sensitive to the constants of the SVV model and are in reasonable agreement with values obtained in experiments.
- The addition of a wall model into the implicit SVV scheme shows enhanced accuracy and enables lower levels of artificial dissipation, which in turn provides a less dissipative bulk flow.

- The study suggests that including wall-modelling can be more important in simulating high-Re wall-bounded flows than the specifics of the subgrid scheme used for large eddy simulations.

Explicit and implicit LES using wall models do not resolve viscous length scales near the wall but show promise in being capable of capturing the outer flow structures. These may include very large-scale motions [33] comprising structures with streamwise extent of order 5–10 pipe diameters. We conclude that both explicit and implicit methods are well suited to simulate circular flows in fully-developed turbulent regimes.

Acknowledgements

The first author would like to thank financial support financial support from the project “Estancias de movilidad en el extranjero José Castillejo para jóvenes doctores” (reference JC2015-00023) of the Spanish “Ministerio de Educación”. Additionally, the authors acknowledge the computer resources and technical assistance provided by the Centro de Supercomputación y Visualización de Madrid (CeSViMa).

References

- [1] Ahn J, Lee JH, Lee J, Kang J, Sung HJ. Direct numerical simulation of a 30r long turbulent pipe flow at $Re_\tau = 3008$. *Phys Fluids* 2015;27(6):065110.
- [2] Asthana K, Jameson A. High-order flux reconstruction schemes with minimal dispersion and dissipation. *J Scientific Comput* 2015;62(3):913–44.
- [3] Beck AD, Bolemann T, Flad D, Frank H, Gassner GJ, Hindenlang F, Munz CD. High-order discontinuous Galerkin spectral element methods for transitional and turbulent flow simulations. *Int J Numer Methods Fluids* 2014;76(8):522–48.
- [4] Berrouk AS, Laurence D, Riley JJ, Stock DE. Stochastic modelling of inertial particle dispersion by subgrid motion for les of high Reynolds number pipe flow. *J Turbulence* 2007;8:1–20.
- [5] Blackburn HM, Sherwin SJ. Formulation of a Galerkin spectral element-Fourier method for three-dimensional incompressible flows in cylindrical geometries. *J Comput Phys* 2004;197(2):759–78.
- [6] Boris JP, Grinstein FF, Oran ES, Kolbe RL. New insights into large eddy simulation. *Fluid Dyn Res* 1992;10(4–6):199.
- [7] Bose ST, Park GI. Wall-modeled large-eddy simulation for complex turbulent flows. *Annu Rev Fluid Mech* 2018;50(1):535–61.
- [8] Brun C, Friedrich R, Silva CBD. A non-linear SGS model based on the spatial velocity increment. *Theoret Comput Fluid Dyn* 2006;20(1):1–21.
- [9] Cheng W, Pullin DI, Samtaney R. Large-eddy simulation of separation and reattachment of a flat plate turbulent boundary layer. *J Fluid Mech* 2015;785:78–108.
- [10] Cheng W, Pullin DI, Samtaney R, Zhang W, Gao W. Large-eddy simulation of flow over a cylinder with re_D from 3.9×10^3 to 8.5×10^3 : a skin-friction perspective. *J Fluid Mech* 2017;820:121–58.
- [11] Chin C, Monty JP, Ooi A. Reynolds number effects in DNS of pipe flow and comparison with channels and boundary layers. *Int J Heat Fluid Flow* 2014;45:33–40.
- [12] Chin C, Ng HCH, Blackburn HM, Monty JP, Ooi A. Turbulent pipe flow at $Re_\tau = 1000$: a comparison of wall-resolved large-eddy simulation, direct numerical simulation and hot-wire experiment. *Comput Fluids* 2015;122:26–33.
- [13] Chin C, Ooi ASH, Marusic I, Blackburn HM. The influence of pipe length on turbulence statistics computed from direct numerical simulation data. *Phys Fluids* 2010;22(11):115107.
- [14] Chung D, Pullin DI. Large-eddy simulation and wall modelling of turbulent channel flow. *J Fluid Mech* 2009;631:281–309.
- [15] Nieuwstadt FTM, den Toonder JM. Reynolds number effects in a turbulent pipe flow for low to moderate Re. *Phys Fluids* 1997;9(11):3398–409.
- [16] Durbin PA. Some recent developments in turbulence closure modeling. *Annu Rev Fluid Mech* 2018;50(1):77–103.
- [17] Ferrer E. An interior penalty stabilised incompressible discontinuous Galerkin-Fourier solver for implicit large eddy simulations. *J Comput Phys* 2017;348:754–75.
- [18] Flad D, Gassner G. On the use of kinetic energy preserving DG-schemes for large eddy simulation. *J Comput Phys* 2017;350:782–95.
- [19] Gassner GJ. An analysis of the dissipation and dispersion errors of the Pn-Pm schemes. *J Scientific Comput* 2013;54(1):21–44.
- [20] Grinstein FF, Margolin LG, Rider WJ. *Implicit large eddy simulation: computing turbulent fluid dynamics*. Leiden: Cambridge Univ. Press; 2007.
- [21] Guala M, Hommema SE, Adrian RJ. Large-scale and very-large-scale motions in turbulent pipe flow. *J Fluid Mech* 2006;554:521–42.
- [22] Hüttel TJ. Direct numerical simulation of turbulent flows in curved and helically coiled pipes. *Comput Fluids* 2001;30(5):591–605.
- [23] Härtel C, Kleiser L, Unger F, Friedrich R. Subgrid scale energy transfer in the near wall region of turbulent flows. *Phys Fluids* 1994;6(9):3130–43.
- [24] Hesthaven JS, Warburton T. *Nodal discontinuous Galerkin methods – algorithms, analysis, and applications*. Springer; 2008.
- [25] Hultmark M, Vallikivi M, Bailey S, Smits AJ. Turbulent pipe flow at extreme Reynolds numbers. *Phys Rev Lett* 2012.
- [26] Inoue M, Mathis R, Marusic I, Pullin DI. Inner-layer intensities for the flat-plate turbulent boundary layer combining a predictive wall-model with large-eddy simulations. *Phys Fluids* 2012;24(7):075102.
- [27] Inoue M, Pullin DI. Large-eddy simulation of the zero-pressure-gradient turbulent boundary layer up to $Re = O(1012)$. *J Fluid Mech* 2011;686:507–33.
- [28] Inoue M, Pullin DI, Harun Z, Marusic I. LES of the adverse-pressure gradient turbulent boundary layer. *Int J Heat Fluid Flow* 2013;44(Supplement C):293–300.
- [29] Karamanos GS. Large eddy simulation using unstructured spectral h/p elements, London: Imperial College; 1999. PhD thesis.
- [30] Karamanos GS, Karniadakis GE. A spectral vanishing viscosity method for large eddy simulations. *J Comput Phys* 2000;163(1):22–50.
- [31] Karamanos GS, Sherwin SJ. A high order splitting scheme for the Navier–Stokes equations with variable viscosity. *Appl Numer Math* 2000;33(1–4):455–62.
- [32] Karniadakis GE, Israeli M, Orszag SA. High-order splitting methods for incompressible Navier–Stokes equations. *J Comput Phys* 1991;97:414–43.
- [33] Kim KC, Adrian RJ. Very large-scale motion in the outer layer. *Phys Fluids* 1999;11:417–22.
- [34] Kirby RM, Sherwin SJ. Stabilisation of spectral h/p element methods through spectral vanishing viscosity: application to fluid mechanics modelling. *Comput Methods Appl Mech Eng* 2006;195(23–24):3128–44.
- [35] Kirby RM, Karniadakis GE. Coarse resolution turbulence simulations with spectral vanishing viscosity–large eddy simulations (SVV-LES). *J Fluids Eng* 2002;124(4):886–91.
- [36] Klewicki J, Chin C, Blackburn HM, Ooi A, Marusic I. Emergence of the four layer dynamical regime in turbulent pipe flow. *Phys Fluids* 2012;24(4):045107.
- [37] Koal K, Stiller J, Blackburn HM. Adapting the spectral vanishing viscosity method for large-eddy simulations in cylindrical configurations. *J Comput Phys* 2012;231(8):3389–405.
- [38] Larsson J, Kawai S, Bodart J, Bermejo-Moreno I. Large eddy simulation with modeled wall-stress: recent progress and future directions. *Mech Eng Rev* 2016;3(1).
- [39] Lee JH, Sung HJ. Comparison of very-large-scale motions of turbulent pipe and boundary layer simulations. *Phys Fluids* 2013;25(4):045103.
- [40] Lundgren TS. Strained spiral vortex model for turbulent fine structure. *Phys Fluids* 1982;25(12):2193–203.
- [41] Maday Y, Ould Kaber SM, Tadmor E. Legendre pseudospectral viscosity method for nonlinear conservation laws. *SIAM J Numer Anal* 1993;30(2):321–42.
- [42] Manzanero J, Ferrer E, Rubio G, Valero E. On the role of numerical dissipation in stabilising under-resolved turbulent simulations using discontinuous Galerkin methods. *arXiv:180510519* 2018.
- [43] McKeon BJ, Li J, Jiang W, Morrison JF, Smits AJ. Further observations on the mean velocity distribution in fully developed pipe flow. *J Fluid Mech* 2004;501:135–47.
- [44] McKeon BJ, Swanson CJ, Zagarola MV, Donnelly RJ, Smits AJ. Friction factors for smooth pipe flow. *J Fluid Mech* 2004;511:41–4.
- [45] Misra A, Pullin DI. A vortex-based subgrid stress model for large-eddy simulation. *Phys Fluids* 1997;9(8):2443–54.
- [46] Monty JP, Stewart JA, Williams RC, Chong MS. Large-scale features in turbulent pipe and channel flows. *J Fluid Mech* 2007;589:147–56.
- [47] Moura RC, Sherwin SJ, Peiro J. Linear dispersion-diffusion analysis and its application to under-resolved turbulence simulations using discontinuous Galerkin spectral/hp methods. *J Comput Phys* 2015;298:695–710.
- [48] Ng HCH, Monty JP, Hutchins N, Chong MS, Marusic I. Comparison of turbulent channel and pipe flows with varying Reynolds number. *Exp Fluids* 2011;51(5):1261–81.
- [49] Pasquetti R. Spectral vanishing viscosity method for LES: sensitivity to the SVV control parameters. *J Turbulence* 2005;6.
- [50] Piomelli U. Wall-layer models for large-eddy simulations. *Prog Aerospace Sci* 2008;44(6):437–46. Large Eddy Simulation - Current Capabilities and Areas of Needed Research
- [51] Piomelli U, Balaras E. Wall-layer models for large-eddy simulations. *Annu Rev Fluid Mech* 2002;34:349–74.
- [52] Pullin DI, Saffman PG. Vortex dynamics in turbulence. *Annu Rev Fluid Mech* 1998;30:31–51.
- [53] Reynolds O. An experimental investigation of the circumstances which determine whether the motion of water shall be direct or sinuous, and of the law of resistance in parallel channels. *Philos Trans R Soc* 1883;174:935–82.
- [54] Sagaut P. *Large eddy simulation for incompressible flows: an introduction*. Scientific computation. Springer; 2001.
- [55] Saito N. Large-eddy simulations of fully developed turbulent channel and pipe flows with smooth and rough walls. California Institute of Technology; 2014. PhD thesis.
- [56] Saito N, Pullin DI. Large eddy simulation of smooth-rough-smooth transitions in turbulent channel flows. *Int J Heat Mass Transf* 2014;78:707–20.
- [57] Saito N, Pullin DI, Inoue M. Large eddy simulation of smooth-wall, transitional and fully rough-wall channel flow. *Phys Fluids* 2012;24(7):075103.
- [58] Sherwin SJ. Dispersion analysis of the continuous and discontinuous Galerkin formulations. In: *International Symposium on Discontinuous Galerkin Methods*. Springer; 1999. p. 425–31.
- [59] Smits AJ, McKeon BJ, Marusic I. High-Reynolds number wall turbulence. *Annu Rev Fluid Mech* 2011;43. 353–75

- [60] Spalart PR. Detached-eddy simulation. *Annu. Rev. Fluid Mech* 2009;41(1):181–202.
- [61] Tadmor E. Convergence of spectral methods for nonlinear conservation laws. *SIAM J Numer Anal* 1989;26:30–44.
- [62] Thomas AZ. On the rotation and skew-symmetric forms for incompressible flow simulations. *Appl Numer Math* 1991;7(1):27–40.
- [63] Wu X, Moin P. A direct numerical simulation study on the mean velocity characteristics in turbulent pipe flow. *J Fluid Mech* 2008;608:81–112.
- [64] Xu C, Pasquetti R. Stabilized spectral element computations of high Reynolds number incompressible flows. *J Comput Phys* 2004;196(2):680–704.
- [65] Zagarola MV, Smits AJ. Mean-flow scaling of turbulent pipe flow. *J Fluid Mech* 1998;373:33–79.
- [66] Zhao R, Smits AJ. Scaling of the wall-normal turbulence component in high-Reynolds-number pipe flow. *J Fluid Mech* 2007;576: 457–73